

**SIMULATION OF LIGHTWAVE PROPAGATION IN PHOTONIC
DEVICES**

by

MOHD HANAPIAH BIN MOHD YUSOFF

**Thesis submitted in fulfillment of the requirements
for the degree of
Doctor of Philosophy**

JUNE 2010

850444

6-7-77

f TA1520

H233

2010

ACKNOWLEDGMENT

بِسْمِ اللَّهِ الرَّحْمَنِ الرَّحِيمِ

My most sincere thanks go to my advisors Associate Professor Haslan Abu Hassan and Associate Professor Md. Roslan Hashim from School of Physics, Universiti Sains Malaysia, for years of support, guidance and patience that have led me to the completion of this research work. I would also like to thank the members of the examining committee for their effort and diligence in reading the manuscript of this thesis.

I also extend my thanks to Universiti Teknologi MARA for providing the necessary facilities during the initial years of part-time research work and for granting me study leave during the final two years. I wish also to thank members of Photonic Research Center in Universiti Malaya for the useful discussions on silica waveguide. And my thanks to Ministry of Science and Technology Malaysia, for financing part of the research work.

Above all, I want to thank my lovely wife, Norizan for her extreme patience and unwavering support and to all my children Fikri Hakim, Aliaa, Aisyah and Adila for believing in me, constantly encouraging me and confidence boosting. I'm also thankful and indebted to my in-laws, Hj. Abdul Ghani Hj. Mahmood and Hajah Zainun Abdullah and to all family members for their support.

Finally but not least, I would like to dedicated my thesis to both my late parents, Hj. Mohd Yusoff Embi and Hajah Amina Mohd Batcha for their years of sacrifice, support and love. Thank you.

TABLE OF CONTENTS

Acknowledgment	ii
Table of Contents.....	iii
List of Tables	viii
List of Figures	ix
List of Abbreviations	xxii
List of Symbols	xxiv
Abstrak	xxx
Abstract	xxxii

CHAPTER 1 – INTRODUCTION

1.0 Introduction.....	1
1.1 Photonic Devices and Integrated Circuits.....	1
1.2 Overview of the Dissertation.....	4
1.2.1 Single Mode Condition in GaAs/AlGaAs Rib Waveguide.....	6
1.2.2 Germanium Dioxide Doped Silica Polarization Rotator.....	7
1.2.3 Low Refractive Index Grating Waveguide Polarization Splitter based on Resonant Tunneling	8
1.2.4 Analysis of Multiple Reflections in Hybrid Photonic Crystal Multimode Interference Coupler.....	9
1.2.5 Hybrid Photonic Crystal Wavelength Division Multiplexer and channel Interleaver.....	10
1.3 Major New Contributions.....	11
1.4 Methodology and Computation Tools used in this Thesis.....	11

CHAPTER 2 - DIELECTRIC WAVEGUIDE THEORY

2.0 Introduction – Maxwell Equations 14

2.1 Dielectric Waveguide 16

 2.1.1 Dielectric Slab Waveguide Modes 19

 2.1.2 Mode Expansion..... 22

2.2 Coupled Waveguide Array 22

 2.2.1 Photonic Band Diagram of 1-D Periodic Structure 24

 2.2.2 Line Defect Modes 27

2.3 2-D Photonic Crystals..... 32

 2.3.1 Maxwell’s Equations in Periodic Media. 33

CHAPTER 3 - COMPUTATIONAL TECHNIQUES IN OPTICAL WAVEGUIDES

3.0 Introduction 36

3.1 Numerical Techniques..... 37

 3.1.1 Finite Difference Method 37

 3.1.2. Finite Element Method 39

3.2 Semi-Analytical Techniques 41

 3.2.1 Effective Index Method 41

 3.2.2 The Film Mode Matching Method 44

3.3 Propagation Techniques 47

 3.3.1 Finite Difference Time Domain (FDTD) Method 47

 3.3.2 Eigenmode Expansion (EME) Method..... 48

3.4 Boundary and Interface Conditions..... 51

3.5 Optimizations 53

3.6 Comparison Between Different Optical Waveguide Propagation Analysis.....54

CHAPTER 4 - SINGLE-MODE CONDITION AND ZERO BIREFRINGENCE
GALLIUM ARSENIDE RIB WAVEGUIDE

4.0 Introduction 56

4.1 Single Mode Condition 57

 4.1.1 Modal Analysis..... 60

 4.1.2 Effective Indices and Power confinement factor (CF) of H_{21}^y and H_{21}^x modes, and lateral single-mode cut-off 64

 4.1.3 Effective Indices and Power confinement factor (CF) of $H_{31}^{x,y}$ and $H_{12}^{x,y}$ modes, and the vertical single-mode cut-off..... 66

 4.1.4 Identification of the First Higher Order Mode and its Confinement Factor.. 68

 4.1.5 The Correction Factor for Single-Mode Condition.....73

4.2 Modal Birefringence and Hybridness of Rib Waveguide 73

 4.2.1 Zero Birefringence Rib Waveguide..... 76

4.3 Summary 81

CHAPTER 5 - GERMANIUM DIOXIDE DOPED SILICA POLARIZATION
ROTATOR

5.0 Introduction..... 83

5.1. Theory 85

 5.1.1 Optimization..... 86

5.2 Structural Enhanced Polarization Birefringence and Hybridness 87

 5.2.1 Symmetrically clad waveguide..... 88

 5.2.2 Asymmetrically clad waveguide 89

5.3 Compact Slanted Silica Polarization Rotator Waveguide 92

 5.3.1 Fabrication Tolerance Analysis Using Finite Element Method 93

5.4 Practical Slanted Waveguide Polarization Rotator Design with Low Transition Loss	102
5.4.1 Propagation Analysis Using Finite Element – Eigenmode expansion (FE-EME) method.....	104
5.5 Summary	107
 CHAPTER 6 - LOW REFRACTIVE INDEX GRATING WAVEGUIDE POLARIZATION SPLITTER BASED ON RESONANT TUNNELLING	
6.0 Introduction.....	108
6.1 Design Principle.....	109
6.2 Optimizing the Coupling Section.....	114
6.3 Results and Discussion	116
6.3.1 Fabrication Tolerance Analysis.....	119
6.4 Summary	120
 CHAPTER 7 - ANALYSIS OF MULTIPLE REFLECTIONS IN HYBRID PHOTONIC CRYSTAL MULTIMODE INTERFERENCE COUPLER	
7.0 Introduction.....	122
7.1 Modal Characteristic of 1-D and 2-D PhC Waveguides.....	124
7.2. Multiple Reflections in Hybrid Photonic Crystal MMI Coupler	127
7.2.1 Field Intensity Patterns Simulated using Bi-directional Eigen-mode Expansion Method.....	132
7.2.2 Transmission Analysis in Single Output Photonic Crystal MMI Coupler	137
7.3. Summary	141

CHAPTER 8 - HYBRID PHOTONIC CRYSTAL WAVELENGTH DIVISION
MULTIPLEXER AND CHANNEL INTERLEAVER

8.0 Introduction 142

8.1 Hybrid 1.31/1.55 μm Wavelength Division Multiplexer 145

 8.1.1 1-D Coupling Section..... 146

 8.1.2 Combined 1-D and 2-D Coupling Section..... 148

8.2 Optimization..... 149

8.3 Hybrid Photonic Crystal Transmission Spectrum 152

 8.3.1 Hybrid Photonic Crystal Wavelength Division Multiplexer 152

 8.3.2 Comparison to a pure 2-D/1-D Photonic Crystal Wavelength Division
 Multiplexer 154

 8.3.3 Hybrid PhC Wavelength Channel Interleaver 156

8.4 The Extinction Ratios of the Hybrid Photonic Crystal Wavelength Division
Multiplexer 158

8.5 Summary 159

CHAPTER 9 - CONCLUSIONS AND FUTURE WORKS.....160

REFERENCES165

APPENDIX A: Computation of 1-D PhC PBG Diagram and Line Defect Waveguide
Modes using Eigenmode Expansion (EME) Method.....179

PUBLICATIONS AND PRESENTATIONS184

LIST OF TABLES

		Page
Table 1.1	Table 1: Functions achieved to date at 1550 nm wavelength in key integrated optical material systems [6].	2
Table 1.2	Table 2: Elemental optical functions and the corresponding ideal integrated optical material system(s) for operation at 1550 nm wavelength [6].	2
Table 2.1	Table 2.1: The effective index for the fundamental mode in 1-D PhC array line defect channels of width 1.1 μm .	29
Table 3.1	Comparison between different propagation technique in optical waveguide [112].	55
Table A1.1	The effective index for the fundamental mode in W2 1-D PhC line defect waveguide.	181
Table A1.2	The effective indices for GaAs 1-D PhC W8, W10 and W14 multimode waveguides.	182

LIST OF FIGURES

	Page
Figure 1.1	Flow chart - general methodology in the design and optimization process. 12
Figure 2.1	A typical symmetric dielectric slab waveguide with its transverse and normal components to the dielectric interface shown as t and n respectively. 15
Figure 2.2	Type of dielectric waveguides. The dielectric constant of the surrounding is assumed to be ϵ_2 , and the dielectric constant of the core, ϵ_1 is assumed to larger than ϵ_2 . 17
Figure 2.3	Light line, radiation modes and the phase space region for guided modes. 18
Figure 2.4	Types of dielectric slab waveguides, (a) Symmetrical waveguide, (b) Asymmetrical waveguide and (c) Anti-reflection resonant optical waveguide (ARROW). 19
Figure 2.5	Typical field profiles of the first four quasi-TM modes supported in a asymmetric slab waveguide shown in Figure 2.4(b). Typical propagation constants of the modes would have its propagation constants, $\beta_0 > \beta_1 > \beta_2 > \beta_3$. 21
Figure 2.6	A typical dispersion diagram for quasi-TM modes in a dielectric slab waveguide: shown in terms of propagation constant and angular frequency. 21
Figure 2.7	Two-dimensional view of arrayed waveguides in parallel made of a layered structure. The direction of wave propagation is 90° normal to the direction of periodicity. 23
Figure 2.8	Mode patterns of orthogonal modes when three parallel waveguides are brought close for directional coupling. (a)–(c): The field profiles for the six lowest-order guided modes for the index structure of three coupled waveguides. (d) The relative magnitudes of $k_x^{(b)}/k$ positioned with respect to $n(x)$, the refractive-index profile of three coupled waveguides [72]. 23
Figure 2.9	A typical dispersion diagram for TM modes in a coupled dielectric waveguide as in Figure 2.8. As the three coupled waveguides are put closer, the three propagation constants diverge from the original value of an isolated waveguide, depicted in Figure 2.6. 24

Figure 2.10	Linear array of dielectric material with high and low refractive index of 1.59 and 1.0.	25
Figure 2.11	Bloch waves (a), (b), (c), (d) and (e), observed at the band edges of the PBG diagram of Figure 2.12(b). They were computed at wavelength of 1.2 μm for five arrays of periodic dielectric slabs.	26
Figure 2.12	Bands of modes in a uniform 1-D PhC array for high index layer of width, $d = 0.5 \mu\text{m}$ and air gap, s equal (a) 0.6, (b) 0.5, (c) 0.4 and (d) 0.3 μm between the high refractive index layers. The shaded regions are the bands of modes and between the bands are the photonic band gap regions. The first, second and third bands of modes were obtained by applying PMC, PEC and PMC boundary conditions respectively, at the symmetry of the outer most dielectric layers.	27
Figure 2.13	Defect channels incorporated in 1-D periodic structure and s_1 is the defect dimension.	28
Figure 2.14	The single-mode 1-D PhC line defect air channel waveguide formed by introducing a row of air layer of width 1.1 μm . Comparisons of the computed modes in the line defect 1-PhC waveguide with respect to different boundary conditions, PMC, PBC and TBC are given in Table 2.1.	29
Figure 2.15	Photonic band diagrams for uniform periodic structures, (a) lattice constant $a = 1 \mu\text{m}$, air gap $s = 0.5 \mu\text{m}$ and dielectric layer of width $d = 0.5 \mu\text{m}$ and (b) lattice constant $a = 0.6 \mu\text{m}$, air gap $s = 0.3 \mu\text{m}$ and dielectric layer of width $d = 0.3 \mu\text{m}$. The dashed-dot lines between the wavelengths of 0.8 μm to 1.6 μm shown in the figures are the defect mode dispersion curve for air defect channel of width 1.1 μm .	30
Figure 2.16	A typical field profiles of modes in an air channel of width 1.1 μm at operating wavelengths (a) 1.0 μm , (b) 1.3 μm and (c) 1.55 μm .	31
Figure 2.17	Basic (a) 1-D, (b) 2D and (c) 3D PhC periodic array [41,77].	32
Figure 2.18	(a) A 3 dimensional representation of a 2-D PhC structures composed of infinite dielectric pillars in square periodic arrays and (b) its representation in 2 dimensions.	32
Figure 2.19	Geometry of (a) a square lattice PhC in real space and (b) its counterpart in reciprocal space. The irreducible Brillouin zone (shaded dark blue) is indicated in (b) [41].	34

Figure 2.20	The first Brillouin zone (shaded dark blue) together with irreducible Brillouin zone (shaded light blue) of a square lattice. The symmetry points at the center (0,0), face (1/2,0) and corner (1/2,1/2) of the irreducible Brillouin zone are conveniently known as Γ , X and M respectively [41].	35
Figure 3.1	Typical dielectric waveguide structures.	36
Figure 3.2	Finite Difference mesh for modeling of a rib waveguide.	38
Figure 3.3	Implementation of a symmetry (mirror) plane to reduce the computational window by half.	38
Figure 3.4	Discretization of (a) vertical and (b) slanted wall rib waveguide. The finite element representation uses triangular mesh.	40
Figure 3.5	The effective index method for the rib waveguide (a) the original rib waveguide, (b) solving the vertical slab problem to define n_{eff1} and n_{eff2} (step 1), (c) solving the equivalent horizontal slab problem for n_{eff} of the whole structure (step 2).	42
Figure 3.6	The effective index method field and modal solution to problem shown in Figure 3.5.	42
Figure 3.7	The waveguide structure is divided into (a) slices and layers where the index is invariant in the x-direction, (b) thinner slices are introduced to accurately model the slanted wall structure.	44
Figure 3.8	Typical field solution to the rib waveguide structure depicted in Figure 3.7. The major field component excited in the waveguide is shown in (a) and (c), and in (b) and (d) the minor field component, respectively. The hybrid nature of the field solution is basically induced at the corner of the vertical wall rib waveguide structure and in (d) we observed an enhancement of the hybridness at the slanted wall rib waveguide. The color legend with normalized amplitude scale is shown at the center between the figures.	47
Figure 3.9	Mode coefficient at waveguide junction [103].	49
Figure 3.10	(a) A multimode interference (MMI) coupler is described by 5 S-matrices, 2 join matrices (B and D) and 3 propagation matrices (A, C and E) and in (b) the computed field profile by EME method [63,103].	50
Figure 3.11	Optical waveguide with (a) Neumann - BC and (b) Dirichlet - BC [65].	52

- Figure 4.1 Structure for (a) Vertical Wall and (b) Trapezoidal Wall Rib Waveguide. 58
- Figure 4.2 The plot shows the cutoff W/H ratios against h/H ratio calculated using Eq. (4.1) with $\alpha = 0.3$ [22], $\alpha = 0.1$ and $\alpha = 0$ [23], for vertical rib waveguide. And for trapezoidal rib waveguide the equations based in references [119] and [120]. Even though the single-mode condition is restricted by Eq. (4.2), but in the figure results are shown from $r = 0.1$ to 1. 59
- Figure 4.3 The GaAs/AlGaAs rib waveguide structure shown with an extra wide computation window used in the mode analysis. 60
- Figure 4.4 (a) The real component of quasi-TE magnetic field H_{12}^y computed with computation window of $200 \times 13 \mu\text{m}$ shown in an intensity plot and (b) contour plot of the same mode but computed using a smaller computational window. The magnetic field is computed for $r = 0.36$, $H = 5 \mu\text{m}$ and $W = 3.43 \mu\text{m}$. The color legend is shown next to Figure 4.4 (a). 61
- Figure 4.5 The quasi-TE modes H_{11}^y , H_{21}^y , and H_{31}^y are shown in intensity and contour plot. The contour plots were computed with a smaller computation window. The magnetic field is computed for $r = 0.9$, $H = 5 \mu\text{m}$ and $W = 11.82 \mu\text{m}$. 62
- Figure 4.6 Effective index against r , h/H ratios. The dispersion curves shown are (a) fundamental quasi-TE H_{11}^y and its higher order modes H_{21}^y , H_{31}^y , H_{12}^y and (b) fundamental quasi-TM H_{11}^x and its higher order modes H_{21}^x , H_{31}^x , H_{12}^x . The slab mode effective indices (TE and TM) are seen as a single dispersion line together with the higher order modes. Inset shown are enlargement at the point where the $H_{12}^{x,y}$ modes depart from the slab mode dispersion curves. 63
- Figure 4.7 The effective index difference of (a) H_{21}^y and its slab mode effective index, (b) H_{21}^x and its slab mode effective index, both plotted against parameter r (h/H ratio) respectively. The effective index difference were computed at wavelength of $1.15 \mu\text{m}$, for rib waveguide dimensions specified by Eq. (4.1) with $\alpha = 0$, 0.1 and 0.3 , shown with solid, dashed-dot and dashed line respectively. 64
- Figure 4.8 Power confinement factors in the rib region calculated for modes (a) H_{21}^y , (b). H_{21}^x 65

- Figure 4.9 The effective index difference of (a) H_{31}^y and H_{12}^y and slab mode effective index, (b) H_{31}^x and H_{12}^x and slab mode effective index, both plotted against parameter r (h/H ratio) respectively. The effective index difference are computed for waveguide dimensions based on Eq. (4.1) with $\alpha = 0, 0.1$ and 0.3 , shown with solid, dashed-dot and dashed line respectively. 66
- Figure 4.10 Power confinement factors in the rib region calculated for modes (a) H_{31}^y and H_{12}^y , and (b) H_{31}^x and H_{12}^x , against parameter r (h/H ratios). 67
- Figure 4.11 Evolution of the guided H_{12}^y mode from the leaky H_{31}^y mode observed at waveguide dimensions specified by Eq. (4.1) with $\alpha = 0.3$. The magnetic field profiles are shown for quasi-TE modes at various parameter r , (a) $h/H = 0.9$, (b) $h/H = 0.5$, (c) $h/H = 0.4$ and (d) $h/H = 0.36$. 68
- Figure 4.12 The effective index difference of $H_{21}^{x,y}$ to $H_{12}^{x,y}$ and $H_{31}^{x,y}$ modes against parameter r (h/H ratio). The dotted line denoted with a zero (0) is the degenerate line where $n_{eff}(H_{21}^{x,y}) = n_{eff}(H_{12}^{x,y})$. The effective index differences are computed for waveguide dimensions based on Eq. (4.1) with $\alpha = 0, 0.1$ and 0.3 , and they are shown with solid, dashed-dot and dotted line respectively. 69
- Figure 4.13 (a) The effective index difference (Δn_{eff}) of the higher order quasi-TE modes, between H_{21}^y and H_{31}^y , H_{12}^y , and (b) The power confinement factor (CF) of the first higher order mode. The plot is shown for single mode AlGaAs rib waveguide calculated with correction factor $\alpha = 0.3$ computed at a wavelength of $1.15 \mu\text{m}$. The numbers on the plots: (a) the effective index difference between the first and second higher order modes in the waveguide, (b) its computed confinement factor. The numbers (dimensionless) on the plots: (a) the effective index difference between the first and second higher order modes in the waveguide, (b) the computed confinement factor of the first higher order mode. 70
- Figure 4.14 (a) and (b) same as in Figure 4.13. The plot shown, is for single-mode AlGaAs rib waveguide specified by Eq.(4.1) with $\alpha = 0.1$, computed at a wavelength of $1.15 \mu\text{m}$. 71
- Figure 4.15 The power confinement factor (CF) of the first higher order mode in rib waveguide with dimensions specified by Eq.(4.1) with $\alpha = 0.3$. The plots are shown for (a) SOI computed at $1.15 \mu\text{m}$, (b) SOI computed at $1.55 \mu\text{m}$, (c) AlGaAs computed at $1.15 \mu\text{m}$ and (d) AlGaAs computed at $1.55 \mu\text{m}$. 72

- Figure 4.16 H-field profile for a rib waveguide with slab height ratio, h/H at 0.5, computed using FEM. 78
- Figure 4.17 (a) The difference in the effective indices between quasi-TE and quasi-TM fundamental modes (b) Hybridness of the quasi-TE fundamental modes for AlGaAs rib waveguides with various parameter r (h/H ratio) = 0.45, 0.48 and 0.52 computed using FEM. 79
- Figure 4.18 (a) The difference in the effective indices between the first and second fundamental modes (b) TE fraction of the first fundamental modes for AlGaAs rib waveguides with various parameter r (h/H ratio) = 0.48, 0.46, 0.44 and 0.42 computed using FMM method. 80
- Figure 4.19 The zero birefringence curve (solid line) shown in a plot of waveguide width W against slab height h for a $5\text{ }\mu\text{m}$ height rib AlGaAs waveguide computed at wavelength of $1.15\text{ }\mu\text{m}$. The single-mode condition, W/H_{cutoff} (dashed-dot) line is based on Soref et.al., [22] and the projected h/H_{cutoff} (blue dashed-dot) line shown from $h = 0$ to $2\text{ }\mu\text{m}$. The circle and diamond points are zero birefringence waveguide dimensions computed using FEM and FMM respectively. 81
- Figure 5.1 A symmetric clad waveguide with GeO_2 doped silica core and pure silica cladding. 88
- Figure 5.2 The figures represent (a) Δn_{eff} and (b) hybridness for waveguides with slant angles 54.74° , 50° and 45° . The values shown on the plots in (a) represent the Δn_{eff} between the quasi-TE and quasi-TM modes, and in (b) the hybridness of the first mode. The red regions are high Δn_{eff} and hybridness regions, whereas the blue/purple regions represent low Δn_{eff} and hybridness regions. 89
- Figure 5.3 An asymmetric clad waveguide with silica substrate and air as top cladding. 90
- Figure 5.4 The figures represent (a) Δn_{eff} and (b) hybridness for waveguides with slant angles 54.74° and 45° . The values shown on the plots in (a) represent the Δn_{eff} between the quasi-TE and quasi-TM modes, and in (b) the hybridness of the first mode. The red regions are high Δn_{eff} and hybridness regions. 90

Figure 5.5	Vector magnetic field of the (a) quasi-TE (H_{11}^y) and (b) quasi-TM (H_{11}^x) modes in the asymmetrically clad silica waveguide with a slanted side wall angle of 46° . The width and height of the waveguide are set at $5.8 \mu\text{m}$ and $8.4 \mu\text{m}$ respectively.	92
Figure 5.6	Half-beat length as a function of waveguide width w . The vertical dotted line shown are for widths $w = 5.8 \mu\text{m}$. The dashed-dot, solid and dashed lines are the half beat-length for waveguides with slanted side wall angles $\theta = 44^\circ, 46^\circ$ and 48° respectively.	94
Figure 5.7	Hybridness of the first mode as a function of waveguide width w . The vertical dotted line shown are for width $w = 5.8 \mu\text{m}$. The dashed-dot, solid and dashed lines are the hybridness for waveguides with slanted side wall angles $\theta = 44^\circ, 46^\circ$ and 48° respectively.	94
Figure 5.8	Polarization conversion in GeO_2 doped silica waveguide as a function of propagation distance. The dashed-dot, solid and dotted lines are the polarization conversion for waveguides with slanted side wall angles $\theta = 44^\circ, 46^\circ$ and 48° respectively.	95
Figure 5.9	Polarization crosstalk as a function of propagation distance for waveguide width $w = 5.8 \mu\text{m}$. The dashed-dot, solid and dotted lines are the crosstalk for waveguides with slanted side wall angles $\theta = 44^\circ, 46^\circ$ and 48° respectively.	96
Figure 5.10	Polarization crosstalk as a function of waveguide width at waveguide propagation distance $z = 770 \mu\text{m}$. The dashed-dot, solid and dotted lines are the crosstalk for waveguides with slanted side wall angles $\theta = 44^\circ, 46^\circ$ and 48° respectively.	97
Figure 5.11	Hybridness and half-beat length L_π as a function of waveguide core refractive index, computed at waveguide width $w = 5.8 \mu\text{m}$ and slanted side wall facet angle of 46° .	98
Figure 5.12	Polarization crosstalk as a function of waveguide core refractive index computed at waveguide width $w = 5.8 \mu\text{m}$ and propagation distance $z = 770 \mu\text{m}$. The dashed-dot, solid and dotted lines are the crosstalk for waveguides with slanted side wall angles $\theta = 44^\circ, 46^\circ$ and 48° respectively.	99
Figure 5.13	Hybridness and half-beat length L_π as a function of waveguide height, computed at waveguide width $w = 5.8 \mu\text{m}$ and slanted side wall facet angle of 46° .	100

Figure 5.14	Polarization crosstalk, and normalized output power of the TM and TE modes as a function of waveguide height computed at width $w = 5.8 \mu\text{m}$, slanted side wall slant facet angle of 46° and propagation distance $z = 770 \mu\text{m}$. The solid line is the polarization crosstalk and the dashed-dot and dotted lines are the TM and TE normalized output power.	100
Figure 5.15	Hybridness of the quasi-TE and quasi-TM modes, h_y and h_x , and half-beat length L_π as a function of operating wavelength, computed at waveguide width $w = 5.8 \mu\text{m}$ and slanted side wall facet angle of 46° .	101
Figure 5.16	Polarization crosstalk, and normalized output power of the TM and TE modes as a function of operating wavelength computed at width $w = 5.8 \mu\text{m}$, slanted side wall slant facet angle of 46° and propagation distance $z = 770 \mu\text{m}$. The solid line is the polarization crosstalk and the dashed-dot and dotted lines are the TM and TE normalized output power.	102
Figure 5.17	Geometry of the polarization rotator design. In Figure 5.17(a), the input/output waveguides are directly coupled to the polarization rotator waveguide section. In Figures 5.17(b) and (c), the coupling of the input/output waveguide to the polarization rotator waveguide is conducted via a tapered slanted waveguide and a twisted waveguide respectively.	103
Figure 5.18	(a) Growth of TM mode component and (b) decay of TE mode component, in the polarization rotator.	104
Figure 5.19	Normalized power curves for TE and TM modes obtained by FE-EME propagation analysis. The total mode power is the total of the TE and TM modes powers in the waveguide.	105
Figure 6.1	The resonant tunneling polarization splitter configuration based on low index grating waveguide.	109
Figure 6.2	The grating waveguide WG1 (WG3) effective indices (circles) shown for (a) TM and (b) TE polarizations, computed for the grating waveguide slab width of $0.5 \mu\text{m}$, with air gap size of $0.1 \mu\text{m}$. the conventional slab waveguide effective index (solid line – diamonds) was computed for waveguide width from $0.4 \mu\text{m}$ to $8 \mu\text{m}$.	110

Figure 6.3	The quasi TM modes (H_{nm}^x) supported in the coupled grating waveguides for the first three vertical modes ($m = 1, 2, 3$). The horizontal orders are shown for $n = 1$ to 5. The surface plots represent the mode's field amplitude supported in the waveguide. Apart from H_{11}^x mode, all the other modes follow normalized scale of the color legend shown next to the H_{12}^x mode.	111
Figure 6.4	The input single-mode waveguide is end-coupled to the three channel waveguide directional coupler.	112
Figure 6.5	Supermodes in the coupling section of the grating waveguide polarization splitter. The modes in Figures 6.5(a), (b) and (c) have effective indices n_1 , n_2 and n_3 respectively.	113
Figure 6.6	Hypercube diagram obtained from the optimization process. Red points denote optimum values for resonator width w and gap g . Optimization conducted using global optimizer.	115
Figure 6.7	Polarization splitter designed with two grating waveguides and an intermediate conventional waveguide (resonator).	116
Figure 6.8	Field intensity of (a) TE polarized light launched into port 1 exiting port 2, and (b) TM polarized light launched into port 1 exiting port 3, computed using quasi 2-D EIM-EME method.	116
Figure 6.9	(a) The transfer coefficient of the TE and TM polarized light launched into port 1. The solid (dashed-dot) line and dotted (dashed) line are the TE (TM) polarized light exiting ports 2 and 3 respectively. (b) The splitting ratio (SR) calculated for TE and TM polarization are shown by solid and dashed lines respectively. Both figures shown are results analyzed against length of coupling section.	117
Figure 6.10	Loss analysis is based on full vectorial H -field computation using finite element with perfectly match layer boundary condition. In the grating waveguide, (a) TM and (b) TE mode losses at waveguide width of $6.5 \mu\text{m}$ are 1.85 dB/mm and 1.93 dB/mm respectively. Mode loss in resonator at slab width of $1.212 \mu\text{m}$ for TM mode is 1.2 dB/mm.	118
Figure 6.11	The splitting ratio for TM (SR_{TM}) and TE (SR_{TE}) modes computed in the fabrication tolerance of the (a) resonator width, (b) resonator's gap, (c) grating waveguide slab width, and (d) grating waveguide gap spacing. The SR value of 13 dB is the minimum acceptable SR for a practical polarization diverse scheme.	119

Figure 6.12	Parameters in the polarization splitter design which were varied in the fabrication tolerance analysis.	120
Figure 7.1	The hybrid PhC model consisting of 1-D PhC multimode interference section and 2-D PhC input/output sections.	124
Figure 7.2	(a) The Bloch mode photonic band diagram for a square lattice 2-D PhC. The band diagram was calculated by planewave expansion method. (b) In the 2-D PhC structure with square lattice of dielectric rods in air. The electric field (E_y) is shown in the y -direction (perpendicular out of plane) together with the magnetic field (H_x) in the x -direction. The wave propagation is in the z -direction. The constants w and a , are the width and lattice constant of the periodic dielectric rods.	125
Figure 7.3	Slab mode photonic band diagram for W8 1-D PhC air channel waveguide. The arrows show the line defect 1-D PhC multimode waveguide supports 4 defect modes at normalized frequency of 0.277 (wavelength of 1.55 μm).	126
Figure 7.4	Mode coefficient at a simple junction between two PhC waveguides.	128
Figure 7.5	(a) Mode coefficients in the three PhC waveguides, and its reflections and transmission at the two junctions between the waveguides (b) a simplified one junction equivalent of Figure 7.5(a), defined by the total reflection and transmission matrices $R_{\text{multi-refl.}}$ and $T_{\text{multi-refl.}}$ in Eqs. (7.5) and (7.6) respectively.	129
Figure 7.6	The input boundary mode (graphically represented) is shown with the excited modes in W8 1-D PhC waveguide. The lateral boundary condition used at the top and bottom of the simulation domain are perfect magnetic conductor (PMC) placed at the line of symmetry of the outer most dielectric structure.	133
Figure 7.7	The field intensity pattern computed for a 2-D model of the hybrid 1-D and 2-D PhC coupler. The image patterns shown on the left and right side were computed with and without the output facet wall (multiple reflections) respectively. The color legend is shown below the figures.	135

- Figure 7.8 The left and right hand side field intensity images are formed by the forward and backward propagating waves, respectively. The computation was conducted with the input/output facet walls, i.e. including effect of multiple reflections. The lengths of the PhC multimode sections are (a) 3.86 μm , (b) 8.51 μm and (c) 7.082 μm . The color legend is shown below the figures. 136
- Figure 7.9 The solid lines represent the normalized transmitted output power computed versus the length of 1-D PhC MMI section, for (a) W8, (b) W10 and (c) W14 multimode PhC waveguide couplers respectively. The smoothly varying dashed lines are the output responses as predicted by multimode interference without the effect of multiple reflection and mode coupling at the input/output junctions. 138
- Figure 7.10 The field intensity profile of (a) W8, (b) W10 and (c) W14 waveguides. The length of the 1-D PhC MMI section shown for all the waveguides is 40 μm . The surface plots of the field intensities follow the same color legend as shown in Figure 7.8. 140
- Figure 8.1 The WDM based on hybrid PhC directional coupler with one row of dielectric rod in between the coupled line defect channel waveguide region. Sections (a) and (b) are the 1-D PhC and 2-D PhC interaction regions respectively. 144
- Figure 8.2 The Bloch mode PBG diagram for the 2-D PhC input/output waveguides. The defect mode dispersion curve is shown as dashed-dot line. The normalized frequencies of 0.277 and 0.328 correspond to the wavelengths 1.55 μm and 1.31 μm . 146
- Figure 8.3 1-D PhC slab mode photonic bandgap diagram computed using EME. The bandgap is between the upper and lower bands of modes. The dashed arrows show two defect supermodes in the coupled line defect 1-D PhC at $f=0.328$ ($\lambda=1.31 \mu\text{m}$) and 0.277 ($\lambda=1.55 \mu\text{m}$) respectively. 147
- Figure 8.4 The odd and even parity modes in the coupled 1-D PhC waveguide at wavelength of 1.55 μm . 147
- Figure 8.5 The coupling length of the 1-D PhC (dashed line) and 2-D PhC (solid line). 148
- Figure 8.6 The optimization curves of the 1-D PhC coupling length. The dashed line is the coupling length at wavelength 1.31 μm and the solid line shown is $2 \times$ coupling length at wavelength 1.55 μm , computed at various waveguide widths. 150

- Figure 8.7 The sections l_1 , l_3 , l_4 and l_5 were optimized for maximum TM modes transmission at $1.31\ \mu\text{m}$ and $1.55\ \mu\text{m}$ exiting port 3 and 2 respectively. 151
- Figure 8.8. The transmission spectrum of a $1.31\ \mu\text{m}/1.55\ \mu\text{m}$ WDM with interaction length $l_1 = 12.33\ \mu\text{m}$ and $l_2 = 2.15\ \mu\text{m}$ calculated by (a) EME and (b) FEM. In both the figures, the dashed and dashed-dot lines are outputs for ports 2 and 3 respectively, as calculated by CMT. The solid and dotted lines are outputs for ports 2 and 3 respectively, as calculated by (a) EME and (b) FEM. 153
- Figure 8.9 (a) The 2-D PhC WDM design. (b) The transmission spectrum of a purely 2-D WDM with interaction length $l = 35a$. In the figure, the dashed and dashed-dot lines are outputs for ports 2 and 3 respectively, as calculated by CMT. And the solid and dotted lines are outputs for ports 2 and 3 respectively, as calculated by EME. 155
- Figure 8.10 (a) The normalized transmitted power of 1-D and 2-D PhC WDM with interaction length $14\ \mu\text{m}$ and $15.23\ \mu\text{m}$ respectively, as shown in Figures 8.10(b) and (c). The dashed and dotted lines represent the transmitted output signals through ports 2 and 3 for the 1-D PhC WDM, respectively. Similarly the solid and dashed-dot lines are the transmitted signals through ports 2 and 3 in the 2-D PhC WDM, respectively. The maximum transmission through ports 2 and 3, are $1.55\ \mu\text{m}$ and $1.31\ \mu\text{m}$ wavelengths respectively. 156
- Figure 8.11 (a) The hybrid PhC directional coupler model used in the simulation of the channel interleaver. (b) The output signals transmission spectrum of the channel interleaver with interaction length $l_1 = 2800\ \mu\text{m}$ and $l_2 = 2.15\ \mu\text{m}$. In figure 8.14(b) the dotted and solid lines are transmitted signal for output ports 2 and 3 respectively, calculated by EME. 157
- Figure 8.12 The field intensity pattern observed in the hybrid WDM with the input pulse excited in port 1 for wavelengths (a) $1.55\ \mu\text{m}$ and (b) $1.31\ \mu\text{m}$ respectively, as computed by FEM. The color legend is shown below the figures. 159
- FigureA1-1 Bloch waves (a), (b), (c) and (d) observed at the band edges of the (e) PBG diagram, were computed at normalized frequency of 0.43 (wavelength at $1\ \mu\text{m}$) for five array of periodic dielectric slabs. At normalized frequency of 0.277 (wavelength at $1.55\ \mu\text{m}$) only the lower band of modes are present. 179

FigureA1-2 The 1-D PhC PBG diagram and the Bloch waves were 180
computed using CAMFR [61]. The first and second bands
of modes were obtained by applying PMC and PEC
boundary condition at the symmetry of the outer most
dielectric layers respectively.

FigureA1-3 The individual slab waveguides are shown with its line of 180
symmetry and the relevant boundary conditions that
preserve its field profiles. The modal field profiles are
shown for (a) first and (b) second modes in the slab
waveguide.

LIST OF ABBREVIATIONS

ARROW	Anti-reflection resonant optical waveguide
AWG	Array waveguide gratings
BC	Boundary condition
BPM	Beam propagation method
CAMFR	Cavity Modelling Framework
CF	Confinement factor
CMT	Coupled mode theory
DWDM	Dense wavelength division multiplexing
EDFA	Erbium doped fiber amplifier
EIM	Effective index method
EME	Eigen-mode expansion
ER	Extinction ratio
FB	Floquet-Bloch
FDM	Finite difference method
FDTD	Finite difference time domain
FE	Finite element
FEM	Finite element method
FMM	Film mode matching
MMI	Multimode interference
OTDM	Optical time-domain multiplexing
PBC	Periodic boundary condition
PBG	Photonic bandgap
PBI	Polarization bit interleaving

PEC	Perfect electric conductor
PhC	Photonic crystal
PIC	Photonic integrated circuits
PMC	Perfect magnetic conductor
PML	Perfectly matched layer
PR	Polarization rotator
PS	Polarization splitter
SOI	Silicon-on-insulator
SR	Splitting ratio
TBC	Transparent boundary condition
TE	Transverse electric
TM	Transverse magnetic
WDM	Wavelength division multiplexers

LIST OF SYMBOLS

<u>Symbol</u>	<u>Definition</u>
AlGaAs	Aluminium gallium arsenide
A	Amplitude
A_r^-	Amplitude coefficient for partly reflected wave
$B_{m,1}^{'+}$	Amplitude coefficient matrix for partly transmitted wave
θ	Angle
ω	Angular frequency
a_m^-, b_m^-	Backward amplitudes of the traveling waves
$[A], [B]$	Band matrix, sparse and symmetric
L_{B_i}	Beat length, and the subscript i is either 1 or 2 representing 1-D or 2-D PhC coupling sections.
E_κ	Bloch wave electric field
σ	Conductivity of material
α	Correction factor in Soref et. al. [22] single mode equation
k_i	Coupling coefficient, and $i = 1$ and 2 , denote the 1-D and 2-D PhC coupling sections respectively.
l'_{c1}, l'_{c2}	Coupling length at 1.31 μm wavelength, subscript 1 and 2 representing 1-D or 2-D PhC coupling sections respectively.
l_{c1}, l_{c2}	Coupling length at 1.55 μm wavelength, subscript 1 and 2 representing 1-D or 2-D PhC coupling sections respectively.
$L_{c,\lambda}$	Coupling length of the coupled section at the respective wavelengths
Γ, M, X	Critical points comprising irreducible Brillouin zone
dB	Decibel
W2, W8, W10, W14	Defect channel waveguide. Denote by W_n where n is the number of defect (or missing) rows

s, s_I	Defect or gap width
∇	Del (nabla) operator
ε	Dielectric constant of material
$\Delta\beta$	Difference in propagation constant
r	Direction of propagation
n_{eff}	Effective index
E_x, E_y, E_z	Electric field components for each rectangular coordinate
E	Electric field vector
Er	Erbium
$ER_{1.55\mu m},$ $ER_{1.31\mu m}$	Extinction ratios (ER) are defined as the ratio of the residue power in the other port as compared to the output power in the desired port. $ER_{1.55\mu m}$ and $ER_{1.31\mu m}$ – extinction ratio at 1.55 μm and 1.31 μm wavelengths.
a_i, a_r, a_{ij}	Field amplitude coefficient
ψ	Field function
a_m^+, b_m^+	Forward amplitudes of the traveling waves
$TE_{frac},$	Fraction of the real Poynting vector flux in TE polarization to the total real Poynting vector flux.
TM_{frac}	Fraction of the real Poynting vector flux in TM polarization to the total real Poynting vector flux.
k_0	Free space wave number
GaAs	Gallium arsenide
GaN	Gallium nitride
Ge	Germanium
GeO ₂	Germanium dioxide
L_π	Half-beat length or the coupling length
h_0, h_x, h_y	Hybridness of the first fundamental mode, quasi-TM and quasi-TE modes respectively.

i	Imaginary constant
InP	Indium phosphide
a	Lattice constant
l_1, l_2, l_3, l_4 and l_5	Lengths of various sections in photonic crystal directional coupler
LiNbO ₃	Lithium niobate
H_x, H_y, H_z	Magnetic field components for each rectangular coordinate
H	Magnetic field vector
μm	Micrometer or micron
$\psi_0^{(1)}(x)$ $\psi_m^{(2)}(x)$	Modal wave-functions in W _a and W _b waveguide section of MMI coupler respectively
A_0^-, B_0^-, C_0^-	Mode coefficient amplitudes in backward direction
A_0^+, B_0^+, C_0^+	Mode coefficient amplitudes in forward direction
D_n	Normal displacement field component
B_n	Normal induction field component
n	Normal vector
f	Normalized frequency, a/λ
P_2, P_3	Normalized power output from ports 2 (1.55 μm output) and 3 (1.31 μm output)
u_k	Periodic function
μ_0	Permeability of free space
ϵ_0	Permittivity of free space
ϕ	Phase constant
P	Phosphorus
d_n	Primitive lattice vector
b	Primitive reciprocal lattice vector

β, β_m	Propagation constant
β_{even_i} and β_{odd_i}	Propagation constant for the even and odd modes, and the subscript i is either 1 or 2 representing 1-D or 2-D PhC coupling sections.
k_x	Wavevector component in x-direction
k_y	Wavevector component in y-direction
P_z	Real Poynting vector flux
\mathbf{k}	Reciprocal lattice vector
x	Rectangular coordinate (x-axis)
y	Rectangular coordinate (y-axis)
z	Rectangular coordinate (z-axis)
R_{00}^i	Reflection coefficient
\mathbf{R}	Reflection matrices
$\left[r^-(l)_{\text{multi-refl.}} \right]_{m,m}$	Reflection matrices in backwards direction including multiple reflections and mode coupling between the excited modes
$\left[r^+(l)_{\text{multi-refl.}} \right]_{m,m}$	Reflection matrices in forward direction including multiple reflections and mode coupling between the excited modes
$\left[R(l)_{\text{multi-refl.}} \right]_{1,m}$	Reflection matrix including multiple reflections and mode coupling
n	Refractive index of material
ϵ_r	Relative dielectric constant
g	Resonator's air gap
Δx	Sampling step of FDTD in x-direction
Δy	Sampling step of FDTD in y-direction
Δz	Sampling step of FDTD in z-direction
Δt	Sampling time interval of FDTD

φ, F, G	Scalar field variable
S_j	Scattering matrix
SiO_2	Silica
Si	Silicon
SiO_xN_y	Silicon oxynitride
r	Slab height over rib height ratio
h	Slab height or waveguide height
d	Slab waveguide thickness
c_0	Speed of light
ρ	Surface charge density
\mathbf{j}	Surface current density
t	Time variable
$[B^-(l)_{\text{multi-refl.}}]_{m,1}$	Total backward propagation modal coefficients matrices including multiple reflections
$\psi_{\text{Total}}(x, z)$	Total fields
$\psi_{\text{Total}}^-(x, z, l)$	Total fields in the backward directions
$\psi_{\text{Total}}^+(x, z, l)$	Total fields in the forward directions
$[B^+(l)_{\text{multi-refl.}}]_{m,1}$	Total forward propagation modal coefficients matrices including multiple reflections
$\mathbf{R}_{\text{multi-refl.}}$	Total reflection matrices including multiple reflections
$\mathbf{T}_{\text{multi-refl.}}$	Total transmission matrices including multiple reflections
$[T']_{m,1}$	Transmission coefficient including mode coupling
\mathbf{T}	Transmission matrices
$[T(l)_{\text{multi-refl.}}]_{1,m}$	Transmission matrix including multiple reflections and mode coupling
∇_t	Transversal nabla operator

t	Transverse component
E_t	Transverse electric field component
H_t	Transverse magnetic field component
$\hat{x}, \hat{y}, \hat{z}$	Unit vector in x, y and z-axes
H	Waveguide/Rib height
W_a, W_b and W_c	Waveguide sections in the photonic crystal MMI coupler
w, W_t, W_b, W	Waveguide width
λ	wavelength
YIG	Yittrium iron garnet

SIMULASI RAMBATAN GELOMBANG CAHAYA DI DALAM PERANTI-PERANTI FOTONIK

ABSTRAK

Disertasi ini adalah tertumpu kepada simulasi rambatan gelombang cahaya dalam peranti fotonik leper, ianya termasuk penyiasatan keadaan satu mod dalam pandu gelombang rusuk, reka bentuk pemutar dan pembelah polarisasi, penyiasatan pantulan berganda dalam pengganding interferens-berganda hablur fotonik dan reka bentuk pembahagi panjang-gelombang hablur fotonik hibrid 1-D dan 2-D dan antara-silih saluran.

Pendekatan yang diambil dalam reka-bentuk adalah menggunakan kaedah separa-analitik, ianya bagi membolehkan penggunaan proses optimisasi pantas. Teknik carian global dan simpleks setempat telah digunakan dengan meluas. Dalam penyiasatan keadaan satu mod dalam pandu gelombang rusuk dan reka bentuk pemutar polarisasi pandu gelombang silika kaedah “film mode matching” dan “finite element” telah digunakan. Kaedah “finite element – eigen mode expansion” digunakan dalam analisa rambatan pemutar polarisasi pandu gelombang silica. Kaedah indeks efektif kuasi 2-D dan “eigen mode expansion” digunakan dalam mereka bentuk pembelah polarisasi pandu gelombang silica, penyiasatan pantulan berganda dalam pengganding interferens-berganda hablur fotonik dan reka bentuk pembahagi panjang-gelombang hablur fotonik hibrid 1-D dan 2-D dan antara-silih saluran.

Secara keseluruhan, kesemua objektif yang ditetapkan dalam tesis ini adalah tercapai. Dalam penyiasatan pandu-gelombang rusuk satu mod dari gallium arsenid/aluminium gallium arsenid (GaAs/AlGaAs), formulasi satu mod bagi pandu gelombang rusuk silikon atas silica didapati adalah juga terpakai kepada pandu-gelombang rusuk GaAs/AlGaAs. Satu kaedah langsung bagi menetapkan had satu

mod dalam arah menegak telah dikenal pasti dengan mengguna faktor kuasa terkurung dalam pandu gelombang tersebut. Peranti-peranti optik berasaskan pandu-gelombang silika bagi tujuan pengawalan polarisasi isyarat telah disiasat. Satu reka-bentuk pemutar polarisasi (TE/TM) menggunakan pandu-gelombang silika telah diperolehi dan panjang peranti tersebut adalah $790\text{ }\mu\text{m}$ dan kecondongan dinding sisinya adalah 46° . Kecekapan peranti tersebut dalam menukar polarisasi adalah 99% dengan nilai “crosstalk” pada -38 dB dengan kecekapan keseluruhan pindahan kuasa dalam lingkungan 81%. Bagi reka-bentuk pembelah polarisasi pandu-gelombang silika, ianya terdiri dari pengganding berarah tiga saluran yang simetrik, ditengahnya adalah pandu-gelombang konvensional dan disebelah luar adalah dua pandu-gelombang parutan. Satu reka bentuk yang padat telah diperolehi dengan panjang keseluruhan peranti tersebut adalah $340\text{ }\mu\text{m}$ dan nisbah pembahagian isyarat polarisasi TE dan TM yang diperolehi adalah 36 dB dan 15 dB masing-masing.

Akhir sekali dalam tesis ini, peranti-peranti optik yang berasaskan hablur fotonik hibrid 1-D dan 2-D telah dicadangkan dan disiasat. Dalam penyiasatan pengganding interferens berganda, kesan dari isyarat pantulan berganda dilihat sebagai sebab utama mengapa imej berkala dalam pengganding tersebut menyimpang dari prinsip pengimejan-diri. Dalam reka-bentuk pembahagi berganda panjang gelombang, satu reka-bentuk yang efisien dan padat telah dicadangkan bagi panjang gelombang $1.31/1.55\text{ }\mu\text{m}$, dengan panjang keseluruhan peranti tersebut adalah $12.33\text{ }\mu\text{m}$. Kecekapan pemindahan kuasa peranti tersebut adalah 91% dan nisbah kepupusan adalah -23.7 dB dan -20.8 dB bagi panjang gelombang $1.31\text{ }\mu\text{m}$ dan $1.55\text{ }\mu\text{m}$ masing-masing. Bagi peranti antara-silih saluran, dengan mengguna panjang interaksi sepanjang $2800\text{ }\mu\text{m}$, ianya menghasilkan renggangan saluran sebesar 0.8 nm dengan kecekapan keluaran sebanyak 90%

SIMULATION OF LIGHTWAVE PROPAGATION IN PHOTONIC DEVICES

ABSTRACT

This dissertation focuses on the simulation of lightwave propagation in planar devices, which include investigation of single mode conditions in rib waveguide, designs of compact silica polarization rotator and splitters, investigation of multiple reflections in photonic crystal (PhC) multimode interference couplers and design of hybrid 1-D and 2-D PhC wavelength division multiplexers and channels interleavers.

In the design approach, we have adopted semi-analytical technique which allows us to incorporate fast optimization process. Global and local simplex search techniques were extensively used. In the investigation of single mode conditions in rib waveguide and the design of silica polarization rotator, full vectorial film mode matching and finite element methods were used. Propagation analysis in the silica polarization rotator was conducted using finite element eigen-mode expansion method. The quasi 2-D effective index method with eigen mode expansion method was used in the design of compact silica grating waveguide polarization splitter, investigation of multiple reflections in hybrid PhC multimode interference coupler and design of hybrid PhC wavelength division multiplexers and channel interleavers.

Basically all the objectives set in the thesis were achieved. In the investigation of single-mode gallium arsenide/aluminium gallium arsenide (GaAs/AlGaAs) rib waveguide, single-mode formulation for silicon on silica is shown to be equally applicable to GaAs/AlGaAs rib waveguide. A direct method of identifying vertical single-mode cut-off limit is also established by using power confinement factor in the waveguide. In the design and optimization of polarization controlling optical components, compact silica polarization rotator and polarization splitter were investigated. A compact silica polarization rotator of length 790 μm

with slanted sidewall angle of 46° was designed. It has an overall conversion efficiency of 99%, with very low crosstalk value of -38 dB and a power transfer efficiency of about 81%. As for the silica polarization splitter it consisted of a symmetric three channel directional coupler, with intermediate conventional waveguide at the center and two grating waveguides on the outside. a compact design was obtained with an overall length of $340\text{ }\mu\text{m}$ and splitting ratio for the TE and TM polarized signals obtained at 36 dB and 15 dB respectively.

Finally in this thesis, optical components based on hybrid 1-D and 2-D photonic crystal structure were proposed and investigated. In the investigation of hybrid photonic crystal multimode interference coupler, the effect of multiple reflections is observed to be one of the main reasons why image periodicity in the couple departs from self-imaging principle. And in the proposed wavelength division multiplexer, an efficient design was proposed for $1.31/1.55\text{ }\mu\text{m}$ wavelength, with a total device length of $12.33\text{ }\mu\text{m}$. Its power transfer efficiency is 91% and extinction ratios of -23.7 dB and -20.8 dB at wavelength $1.31\text{ }\mu\text{m}$ and $1.55\text{ }\mu\text{m}$ respectively. For the channel interleaver, an interaction length of $2800\text{ }\mu\text{m}$ give a channel spacing of 0.8 nm wavelength, with output efficiency of 90%.

CHAPTER 1

INTRODUCTION

1.0 Introduction

Photonics is the science and technology of generating and controlling photons, particularly in the visible and near infra-red light spectrum. Photonics as a science is closely related to quantum optics and optoelectronics. The emergence of photonic in communications and other applications are largely due to the advent of semiconductor laser (1960's) [1] and low loss optical fibers (1970's) [2]. Especially in telecommunication it is helped further by the development of erbium doped fiber amplifier (EDFA) [3,4] in 1987 and dense wavelength division multiplexing (DWDM) [5] in the 1990's.

1.1 Photonic Devices and Integrated Circuits

Photonic devices lie at the heart of the optical communications revolution. Major photonic devices include optical fibers/waveguides, couplers, electro-optic devices, magneto-optic devices, acousto-optic devices, nonlinear optical devices, optical amplifiers, lasers, light-emitting diodes, and photodetectors. Development and progress in these devices have been achieved not on single material platform but on many different materials, shown in Tables 1 and 2 [6].

Optical components are built using materials including indium phosphide (InP), gallium arsenide (GaAs), lithium niobate (LiNbO_3), silicon (Si), silica-on-silicon (SOI) and organic polymer. Lithium niobate offers little practical promise as a material platform for integration since it cannot be used to practically implement active opto-electronic components like lasers and detectors.

Table 1.1: Functions achieved to date at 1550 nm wavelength in key integrated optical material systems [6].

Material System	Lasers	Amplifiers	Detectors	Modulators	Polarization Controllers	Couplers	Filters	Switches	Attenuators	Isolators	Wavelength Converters	Chromatic Dispersion Compensators	PMD Compensators
Silica [SiO ₂]	X	X			X	X	X	X	X			X	X
Silicon [Si]	X	X	X	X	X	X	X	X	X				
Silicon Oxynitride [SiO _x N _y]					X	X	X	X	X				
Polymers	X	X	X	X	X	X	X	X	X			X	X
Lithium Niobate [LiNbO ₃]	X	X	X	X	X	X	X	X	X		X		X
Indium Phosphide [InP]	X	X	X	X		X	X	X	X		X		
Gallium Arsenide [GaAs]	X	X	X	X		X	X	X	X				
Garnets [e.g. YIG]										X			

Table 1.2: Elemental optical functions and the corresponding ideal integrated optical material system(s) for operation at 1550 nm wavelength [6].

Elemental Optical Function	High Performance Material System
Lasers	InP/GaAs
Amplifiers	Er-doped Silica, InP/GaAs
Detectors	InGaAs
Modulators	LiNbO ₃ , InP
Polarization Controllers	LiNbO ₃
Couplers/Splitters/Combiners/Taps	Silica, Polymers
Multiplexer/Demultiplexer	Silica, Silicon Oxynitride
Tunable Notch Filters	Polymers
Switches	Polymers
Attenuators	Polymers
Isolators	Garnets
Circulators	Garnets
Wavelength Converters	LiNbO ₃ , InP/GaAs
Chromatic Dispersion Compensators	Silica, Silicon, Polymers
PMD Compensators	Polymers, LiNbO ₃

Although active opto-electronic devices can be implemented on GaAs, the intrinsic band-gap of GaAs generally only allows operation in the 850 nm telecommunication wavelength window, limiting its usefulness to local area network applications. Indium phosphide [7] and recently silicon [8], has demonstrated the ability to integration of both active and passive optical devices operating in the 1310 nm or 1550 nm telecommunication wavelength windows, since it supports all the key high-value opto-electronic functions required in an optical transport to be integrated on a single substrate.

In silica-on-silicon technology, waveguide is formed in a silica layer by doping it with phosphorus or germanium atoms. Low-loss integrated silica waveguides on silicon allow for low loss coupling with optical fibers and are used to form a variety of planar lightwave circuits for optical branching, switching and filtering. Silica waveguides can also be used as platforms (motherboards) for hybrid optoelectronic integration [9]. Increases in integration density with this technology are restricted however, by the large minimal bending radius of silica waveguides that is of the order of a few centimeters. A significant denser integration has been demonstrated with higher index contrast silicon oxynitride (SiON) technology [10]. An index contrast in the order of 3.3% between the core of the SiON waveguide and silica cladding, allows the minimum bending radius to be reduced to below 1 mm. Further scaling is possible with silicon-on-insulator technology, where the waveguide is formed in a thin silicon layer. Extremely high refractive index contrast between the silicon core ($n = 3.5$) and silica cladding ($n = 1.444$) allows the waveguide core to be shrunk down to a submicron cross-section, while still maintaining single mode propagation at telecommunications wavelengths. Such extreme light confinement allows the minimal bending radius to be reduced to the micron range, opening an avenue to realize ultra-dense photonic integrated circuits on a single silicon chip [11]. However it also results in significantly enhanced propagation losses due to increased interaction of the waveguiding mode with the sidewall surface roughness [12].

In recent years, organic photonic polymeric materials have undergone rapid development and have exhibited large improvements in performance. Organic polymer waveguide do not have the limitation due to intrinsic bandgap as in group III-IV semiconductor material such as GaAs and InP, making it suitable for wide range of wavelength including blue light generated by gallium nitride (GaN) laser.

Complex switching and routing circuits with state-of-the-art performance have been demonstrated on a polymer waveguide platform. Organic photosensitive polymeric materials offer low cost, flexibility of design and fabrication, and performance suitable for photonic devices [13].

Extensive research is also currently being done on photonic crystal (PhC) integrated circuits [14]. Light propagating in one or two dimensional, periodically coupled, waveguiding structures shows effects that are not observed in bulk media. The new degrees of freedom that arise due to the micro structuring of optical sample allow for almost arbitrary tailoring of the dispersion relation, according to specific needs of device. For higher power of the optical excitation, nonlinear effects broaden the diversity of observable phenomena that arise due to the interaction of the nonlinearity and the unique features of the dispersion relation. Infiltration of these periodic structures with polymers or chemical substance [15,16] added a further ability to manipulate the dispersion properties using electro or acoustic optical effect.

1.2 Motivations and Objectives in the Thesis

The motivation to explore planar optical waveguide technology started with the national top-down project in the year 2002 [17]. And the basic structure that is vital to the design and fabrication of photonic devices is the photonic waveguide. Therefore the goal and scope of this thesis is to conduct theoretical investigation on the propagation of lightwave in photonic waveguides and devices. The basic waveguide structures identified for investigations are the gallium arsenide/aluminium gallium arsenide (GaAs/AlGaAs) rib waveguide and silica channel waveguide. In this thesis the single mode condition was studied in GaAs/AlGaAs rib waveguide by investigating the lateral and vertical higher order modes, the

polarization birefringence of the fundamental polarized modes and compared some of these results with the silicon on insulator (SOI) rib waveguide properties available in literature. Similarly for the silica waveguide, basic properties such as modal birefringence and hybridness due to structural deformation were investigated. Based on these results, polarization controlling devices such as polarization rotator and polarization splitter in silica waveguide were designed and characterized. Further enhancement in the polarization birefringence property was obtained by using the slotted waveguide structure [18,19]. The silica polarization splitter was designed and characterization based on slotted silica waveguide structure.

As a natural progression, the slotted structures were investigated further. The slotted array structures are periodic in nature, however a full 3-D propagation analysis of these structures are very memory intensive and in order to reduce the computer resources required, only a 2-D effective index analysis was conducted on the periodic structure. Models for the multimode interference coupler, wavelength division multiplexer and channel interleavers based on 1-D and 2-D photonic crystal structures consisting of gallium arsenide (GaAs) dielectric rods in air were investigated. The waveguiding in these structures are in the air defect channel waveguide due to bandgap mirror confinement [20]. In real practical devices however it would be based on finite height columns of rods with omni-directional reflectors above and below the structure [21].

As an overview to this thesis, following the introduction given in chapter 1, chapter 2 gives some literature background about electromagnetic wave theory and chapter 3 gives the computational aspect used in this thesis. In the proceeding chapters, the optical waveguide and devices investigated are the single mode condition in large GaAs/AlGaAs rib waveguide, design and optimization of silica

based polarization controlling devices such as polarization rotators and splitters, the effect of multiple reflections in multimode photonic crystal waveguide coupler and finally the design of wavelength division multiplexer and channels interleaver for dense wavelength division multiplexers based on photonic crystal directional coupler. The following sections below summarized the motivations, objectives and results of these research topics and full report are found in chapters 4, 5, 6, 7 and 8 respectively. Finally a conclusion on the research work presented in this thesis and future extension of these works are given in chapter 9.

1.2.1 Single Mode Condition in GaAs/AlGaAs Rib Waveguide.

In chapter 4, single mode condition in gallium arsenide/aluminium gallium arsenide (GaAs/AlGaAs) rib waveguide was investigated. Rib waveguide is important optical device due to its ability to propagate light in single mode at large size comparable to single mode fibre. This would allow better power transfer between rib waveguide and single mode fiber optic, since the spot size of the lightwave are comparable [22,23].

In the single-mode condition in rib waveguide, various formulations such as one proposed by Soref et. al. [22] and Pogossian et. al. [23] were analysed. Even though these formulations are for silicon on insulator (SOI) rib waveguides, its validity to GaAs/AlGaAs rib waveguide was investigated. Therefore one of the objectives in the study of GaAs/AlGaAs rib waveguide was to investigate the single-mode cut off conditions, i.e. the maximum allowable width and slab height that maintain only single-mode propagation in the waveguide. Comparison were made between the effective indices of the modes in the waveguide, specifically the quasi-TE (H_{11}^y , H_{21}^y , H_{31}^y and H_{12}^y) modes to the slab mode effective index. The second

objective was to analysis the power confinement factors of the higher order (H_{21}^y , H_{31}^y and H_{12}^y) modes.

The result obtained shows that the formulation given by Soref et. al. [22] is valid for GaAs/AlGaAs rib waveguides. It is observed that at single-mode GaAs/AlGaAs rib waveguide dimensions, only the fundamental mode effective index is larger than the slab waveguide mode effective index. And in the analysis of the power confinement factor, as the higher order modes evolve from leaky modes into guided modes, the power confined in the rib waveguide due to these modes would increase drastically, thus the results leads to a simple identification of the vertical (slab height) single mode cutoff. Investigation was also conducted to identify polarization independent rib waveguide structures. In a polarization independent rib waveguide, the fundamental quasi-TE and quasi-TM modes effective indices would be the same. Two optical waveguide's mode solving methods were employed in the investigation, the semi analytical film mode matching (FMM) method [24,25] and a full numerical finite element method (FEM) [26].

1.2.2 Germanium Dioxide Doped Silica Polarization Rotator.

One of the most important polarization controlling device in optical integrated circuit is the polarization rotator [27]. It is being used for example to improve isolation between signals in adjacent communication channels in optical transmission system, and by implementing polarization mode interleaving [28] in long distance transmission network. These applications require efficient on-chip polarization rotator that can be integrated with other optical components. Numerous design have been proposed [27,29-32], but in this thesis the design and optimization

of silica polarization rotator based on slanted sidewall waveguide [27] was adopted due to its high conversion efficiency compared to other designs.

Therefore the objectives in chapter 5 were to investigate the effect of structural deformations (variation in width, height and slant angle) on the polarization rotation properties of a germanium doped silica waveguide, and to design and optimize a compact silica waveguide polarization rotator. The polarization rotator properties studied were the hybridness and polarization birefringence. As a results from this study, a polarization rotator design that is highly efficient and tolerant to fabrication errors, was obtained with a slanted structure with sidewall angle of 46° , height and width of $8.4\ \mu\text{m}$ and $5.8\ \mu\text{m}$ respectively. In the fabrication tolerance analysis, the critical parameter observed are the variation in the slant angle of the waveguide sidewall, where as the polarization rotator response is observed to be relatively stable with respect to the variation in the operating wavelengths. The optimum polarization rotator design obtained for operating wavelength of $1.55\ \mu\text{m}$ consisted of a rotator waveguide section, with an intermediate tapered slanted section to facilitate a better power transfer between the input/output sections and the rotator section. The overall polarization conversion and power transfer efficiencies are about 99% and 80% respectively.

1.2.3 Low Refractive Index Grating Waveguide Polarization Splitter based on Resonant Tunneling.

In optical communication system, components based on polarization diverse scheme [33] would have the incoming optical signal split into TE and TM polarized state. One of the polarized states is then rotated and recombined using a power combiner. Splitting of optical signal into its respective polarization components is performed by a polarization splitter. Polarization splitters are based on different

principles [34-37] and these devices mainly utilize material with high refractive indices thus realizing a short and compact device due to its large polarization birefringence. Silica waveguide due to its low refractive index contrast would have low polarization birefringence thus the design of polarization splitters is normally rather large. In this work by the incorporation of slotted or grating structure [38], it enhances the difference in effective indices of the two polarization states therefore a short and compact silica waveguide polarization splitter may be achieved.

The objectives in chapter 6 were to implement the design of a short and compact silica waveguide polarization splitter based on resonant tunneling [37] and to investigate its fabrication tolerance and loss analysis. In the design process, quasi 2-D effective index method with global and local search method is employed to obtain the optimum design. In the polarization splitter design obtained the overall transmission efficiencies for the splitting of TM and TE optical components at a wavelength of 1.55 μm are 88% and 83% respectively.

1.2.4 Analysis of Multiple Reflections in Hybrid Photonic Crystal Multimode Interference Coupler.

In this topic, multiple reflections in hybrid 1-D and 2-D gallium arsenide photonic crystal [39-41] multimode waveguides was investigated. In conventional multimode waveguide, self-imaging [42] is one of the most important phenomena observed. It is being exploited to design and fabricate numerous optical devices [42-44]. However in photonic crystal multimode waveguide where the wave confinement is due to bandgap confinement [20], the reflectivity of all the modes in the waveguide is very large at the end facet of the waveguide. Therefore the objectives in chapter 7 were to investigate the lightwave propagation in multimode photonic crystal waveguide, and the effect of multiple reflections on self-imaging phenomena. And it

is observed that multiple reflections are one of the main reasons why image periodicity in photonic crystal multimode interference coupler departs from self-imaging principle.

1.2.5 Hybrid Photonic Crystal Wavelength Division Multiplexer and Channel Interleaver.

Wavelength selective components in optical communication system are used for wavelength multiplexing/demultiplexing of signals. In conventional optical waveguide structure, wavelength division multiplexer and channels interleaver may be realized in a form such as an array waveguide grating [45] and cascaded Mach-Zehnder interferometer [46] respectively. In photonic crystal structure, numerous design of highly compact wavelength selective components has been reported. They are based on superprism [47,48], couple cavity waveguide [49], mini stopband effect [50,51], and directional couplers [21,52].

For directional couplers based on 2-D photonic crystal, if the total length are large they are not suitable for channel interleaving application since a 2-D photonic crystal waveguide device exhibits relatively high propagation loss [53]. However 1-D photonic crystal waveguide exhibit lower loss [54,55]. Therefore in chapter 8, the objectives were to design and optimize a hybrid 1-D and 2-D gallium arsenide photonic crystal air defect channels wavelength division multiplexer for 1.31/1.55 μm and channels interleaver suitable for dense wavelength multiplexer. In this design, a coupled 1-D photonic crystal air defect channels was used in the interaction region sandwiched between input/output 2-D photonic crystal waveguides. The 2-D photonic crystal section was incorporated due to its superior wave bending efficiency [56,57]. An efficient design with power transfer efficiency of 91% and its extinction ratios of -23.7 dB and -20.8 dB at wavelength 1.31 μm and 1.55 μm respectively,

were obtained. And for the design of dense wavelength division multiplexer's channels interleaver with channel spacing of 0.8 nm wavelength, the power output efficiency obtained is about 90%.

1.3 Major New Contributions

New contributions in this thesis are:

1. Investigation of vertical mode cut-off in large GaAs/AlGaAs rib waveguide using the analysis of power confined in the rib section of the waveguide.
2. Optimum and efficient silica polarization rotator design based on conventional slanted waveguides are presented.
3. Design and characterization of a compact silica polarization splitter based on resonant tunneling effect and grating waveguide.
4. Computation of photonic band diagram for 1-D photonic crystal using quasi 2-D effective index -eigenmode expansion method is introduced.
5. Investigation of lightwave propagation and multiple reflections in photonic crystal multimode interference couplers.
6. Design of a hybrid 1-D and 2-D GaAs photonic crystal wavelength division multiplexer for 1.31/1.55 μm channel splitting and channels interleaver suitable for dense wavelength division multiplexing application with 0.8 nm wavelength spacing.

1.4 Methodology and Computation Tools used in this Thesis

This dissertation blends two types of lightwave simulations i.e. theoretical investigation of physical phenomena and design of photonic waveguide devices. The investigations of physical phenomena include investigation of single mode conditions

in rib waveguides and multiple reflections in photonic crystal multimode interference couplers. Photonic waveguide devices proposed include the compact silica waveguide polarization rotators, silica grating waveguide polarization splitters and the modeling of hybrid 1-D and 2-D photonic crystal wavelength division multiplexer and channels interleaver suitable for dense wavelength division multiplexer. In the design and investigation of the photonic waveguide devices, advanced optimization technique using global and local simplex algorithm were employed [58-60]. A combination of semi-analytical methods [61-63] to design and optimize, and numerical technique [64] in the verification of the designs were used. The general methodology adopted in the design and optimization process is given by the flow chart shown in Figure 1.1.

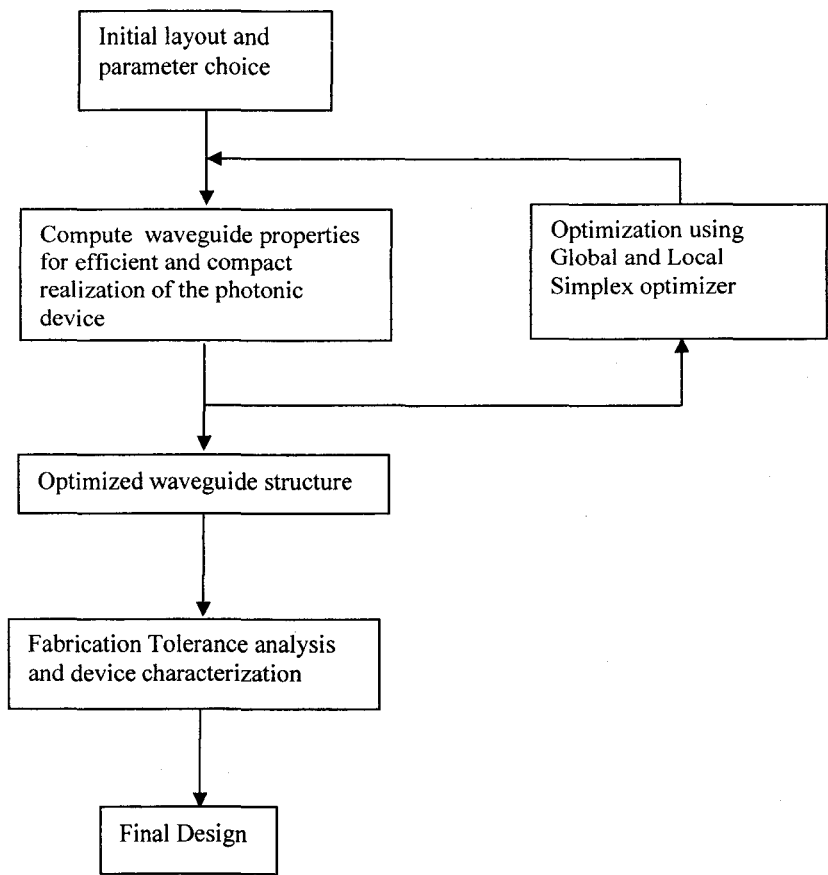


Figure 1.1: Flow chart - general methodology in the design and optimization process.

Photonic softwares used in this thesis, are FIMMWAVE, FIMMPROP [63] and KALLISTOS [60] from Photon Design, CAMFR [61] which is freely available in the internet, and also multiphysics simulation tool Comsol v. 3.4 [64] that is based on finite element analysis. The propagation analyses employed are the quasi 2-D effective index method with eigenmode expansion (EIM-EME) [63] and 3-D finite element method with eigenmode expansion (FE-EME) [63].

CHAPTER 2

DIELECTRIC WAVEGUIDE THEORY

2.0 Introduction – Maxwell Equations

Guided wave optical devices form the basis of modern optical communication systems. The basic physics governing these devices are the Maxwell equations [65-67]. The four underlying Maxwell equations for electromagnetic fields in a source free, non-magnetic medium are

$$\nabla \times \mathbf{E} = -\mu_0 \left(\frac{\partial \mathbf{H}}{\partial t} \right) \quad (2.1)$$

$$\nabla \times \mathbf{H} = \varepsilon_0 \varepsilon_r \left(\frac{\partial \mathbf{E}}{\partial t} \right) \quad (2.2)$$

$$\nabla \cdot \varepsilon_0 \varepsilon_r \mathbf{E} = 0 \quad (2.3)$$

$$\nabla \cdot \mu_0 \mathbf{H} = 0 \quad (2.4)$$

In Eqs. (2.1) – (2.4), \mathbf{E} is the electric field intensity vector and \mathbf{H} is the magnetic field intensity vector, and the operator ∇ is defined as

$$\nabla = \frac{\partial}{\partial x} \hat{x} + \frac{\partial}{\partial y} \hat{y} + \frac{\partial}{\partial z} \hat{z} \quad (2.5)$$

The constants in Maxwell equations are the dielectric constant of free space,

$$\varepsilon_0 = \frac{1}{c^2 \mu_0} \approx \frac{1}{36\pi} \times 10^{-9} \text{ F/m}$$

The permeability of free space, $\mu_0 = 4\pi \times 10^{-7} \text{ H/m}$ and the quantity c is the velocity of light in vacuum.

Taking the curl ($\nabla \times$) of Eq. (2.1) and substituting Eq. (2.2) yields an equation that depends only on the electric field intensity vector \mathbf{E}

$$\nabla \times \nabla \times \mathbf{E} = -\mu_0 \epsilon_0 \epsilon_r \frac{\partial^2 \mathbf{E}}{\partial t^2} \quad (2.6)$$

$$\text{Using the identity} \quad \nabla \times \nabla \times \mathbf{E} = \nabla(\nabla \cdot \mathbf{E}) - \nabla^2 \mathbf{E} \quad (2.7)$$

and substituting in Eq. (2.6), yields the wave equation

$$\nabla^2 \mathbf{E} - \mu_0 \epsilon \frac{\partial^2 \mathbf{E}}{\partial t^2} = 0 \quad (2.8)$$

Considering only time harmonic fields with the time dependence represented by the real part of $\exp(i\omega t)$, results in the time harmonic wave equation

$$\nabla^2 \mathbf{E} + n^2 k_0^2 \mathbf{E} = 0 \quad (2.9)$$

where $n = \sqrt{\epsilon_r} = \sqrt{\frac{\epsilon}{\epsilon_0}}$ is the refractive index, and $k_0 = \omega \sqrt{\mu_0 \epsilon_0}$ the wavenumber of free space. The dielectric constant of the medium $\epsilon = \epsilon_0 \epsilon_r$, where ϵ_r is the relative dielectric constant.

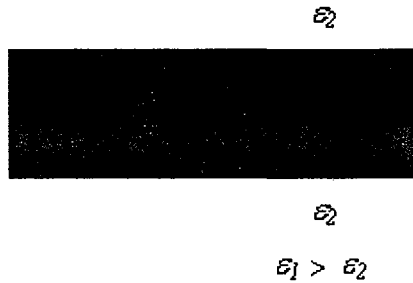


Figure 2.1. A typical symmetric dielectric slab waveguide with its transverse and normal components to the dielectric interface shown as t and n respectively.

At the boundary between the two media, shown in Figure 2.1, distinguish by the dielectric constants ϵ_1 and ϵ_2 , in the absence of charge and current, the boundary conditions on the electric field component transverse (t) and electric displacement component normal (n) to the dielectric interface are

$$E_{1t} = E_{2t} \quad (2.10)$$

$$D_{1n} = D_{2n} \quad (2.11)$$

Hence the electric field normal component becomes, $\epsilon_1 E_{1n} = \epsilon_2 E_{2n}$.

Similarly, the boundary conditions on the magnetic field components transverse and normal to the interface are

$$H_{1t} = H_{2t} \quad (2.12)$$

$$B_{1n} = B_{2n} \quad (2.13)$$

For a non magnetic material, $\mu_r = 1$, the normal magnetic field component, $H_{1n} = H_{2n}$

2.1 Dielectric Waveguide

Waveguides come in variety of different forms: slab waveguide, rectangular waveguide and circular waveguide in the form of optical fiber and holey fibers. The cores are assumed to have an average refractive index (dielectric constant, ϵ_1) higher than the cladding's (surrounding's) refractive index (dielectric constant ϵ_2). In the absence of conducting boundaries, electromagnetic fields exist both inside and outside the dielectric waveguide. The relative amount of energy propagating inside the core increases with an increase in the refractive index contrast between the core and the cladding. Considering the number of different waveguide structures [67,68], we present our discussion based on the simplest type waveguide: the dielectric slab waveguide.

Some of the typical dielectric waveguides are shown in Figures 2.2 (a)-(d): (a) slab dielectric waveguide [69], (b) rectangular dielectric waveguide [69], (c) circular dielectric waveguide (optical fiber) [69] and (d) holey circular dielectric waveguide (holey fiber) [70].

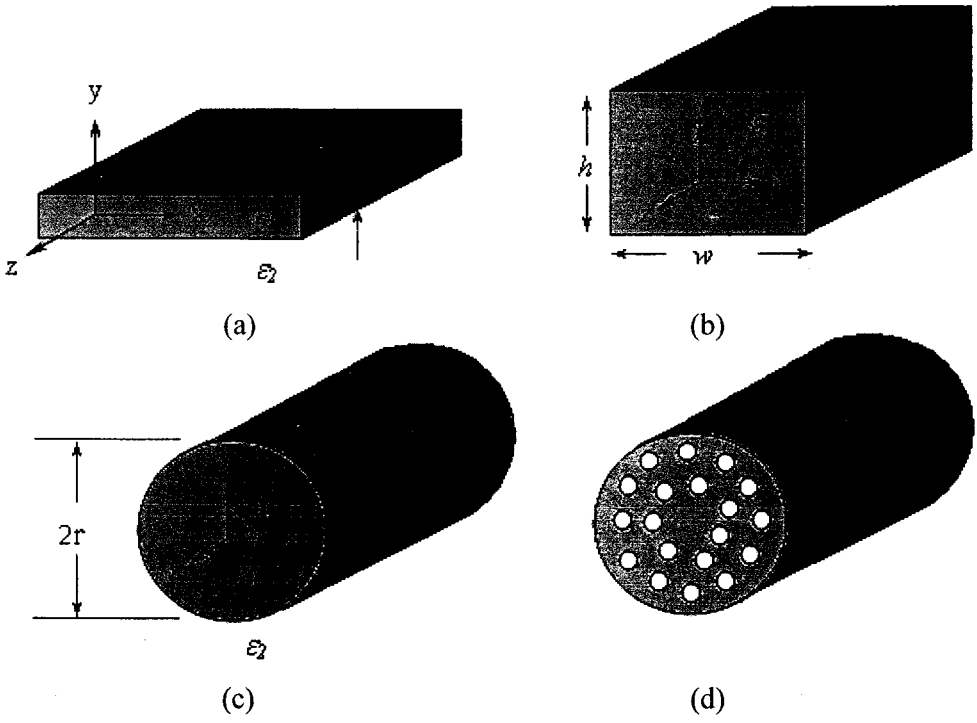


Figure 2.2. Type of dielectric waveguides. The dielectric constant of the surrounding is assumed to be ϵ_2 , and the dielectric constant of the core, ϵ_1 is assumed to be larger than ϵ_2 .

For a general waveguide structure that propagates light along the z -direction, the dielectric constant can be written as $\epsilon(x,y)$, ie. the dielectric function is invariant along the direction of propagation. The field solutions for Maxwell equations are called modes and may be written in the following forms:

$$E(x, y, z, t) = E(x, y) \exp(-i\beta z + i\omega t) \quad (2.14)$$

$$H(x, y, z, t) = H(x, y) \exp(-i\beta z + i\omega t) \quad (2.15)$$

These solutions or modes, would maintain their shape as the field propagates along the z -direction. Each mode is also characterized by its frequency ω , and its wavevector along the z -direction β (also known as propagation constant). The relation between the frequency and the propagation constant along the z -direction defines the dispersion relation.

For a structure with uniform dielectric constant ϵ , Eq. (2.14) and (2.15) can also be written as

$$E(x, y, z, t) = E \exp(-ik_x x - ik_y y) \exp(-i\beta z + i\omega t) \quad (2.16)$$

$$H(x, y, z, t) = H \exp(-ik_x x - ik_y y) \exp(-i\beta z + i\omega t) \quad (2.17)$$

where
$$\epsilon\mu_0 \frac{\omega^2}{c^2} = k_x^2 + k_y^2 + \beta^2 \quad (2.18)$$

and k_x and k_y are the wavevector components along the x and y directions.

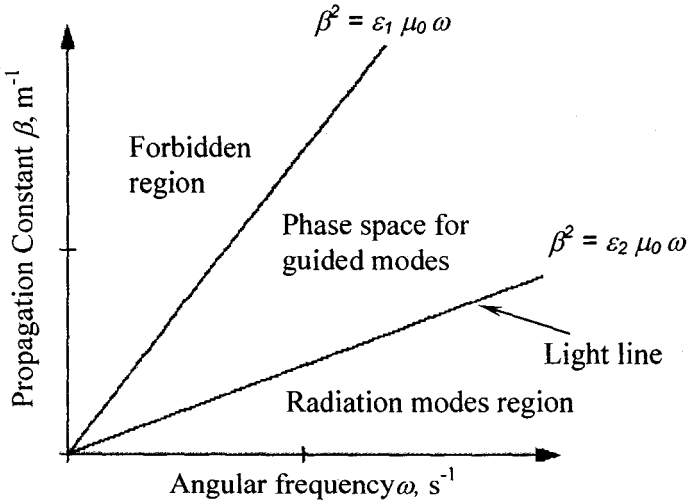


Figure 2.3. Light line, radiation modes and the phase space region for guided modes.

Figure 2.3 shows that for a waveguide structure as shown in Figure 2.2(a), total internal reflection occurs when $\epsilon_2\mu_0 \frac{\omega^2}{c^2} < \beta^2$, in which case the field decays exponentially outside the guiding layer. Thus in the β - ω plane, the guided modes can only exist in the phase space region above the light line of the cladding media. A further constraint imposed on allowed modes is the propagation constant is always less than the core light line, $\epsilon_1\mu_0 \frac{\omega^2}{c^2} > \beta^2$. Thus the allowed phase space region for

guided modes exist between two straight line that go through the origin in the β - ω plane. The propagation constant is related to the effective index of the modes by the relation $n_{eff} = \beta/k_0$, and the effective index of the guided modes based on the above results must be between the range $n_1 > n_{eff} > n_2$, where $n = \sqrt{\epsilon_r}$.

2.1.1 Dielectric Slab Waveguide Modes

The slab waveguide supports a finite number of guided modes, leaky modes and infinite continuum of radiation modes. The guided modes, leaky modes and the radiation modes have to satisfy the wave equation, and can be obtained as solutions of a boundary value problem. Figure 2.4 shows different type of dielectric slab waveguides, symmetrical slab waveguide, asymmetrical slab waveguide and anti-reflection resonant optical waveguide (ARROW) [20], which supports guided leaky modes. The refractive indices of the different layers are given by n_1 , n_2 , n_3 and n_4 , and the thickness of the core (wave-guiding) layer shown with refractive index n_1 is $2d$.

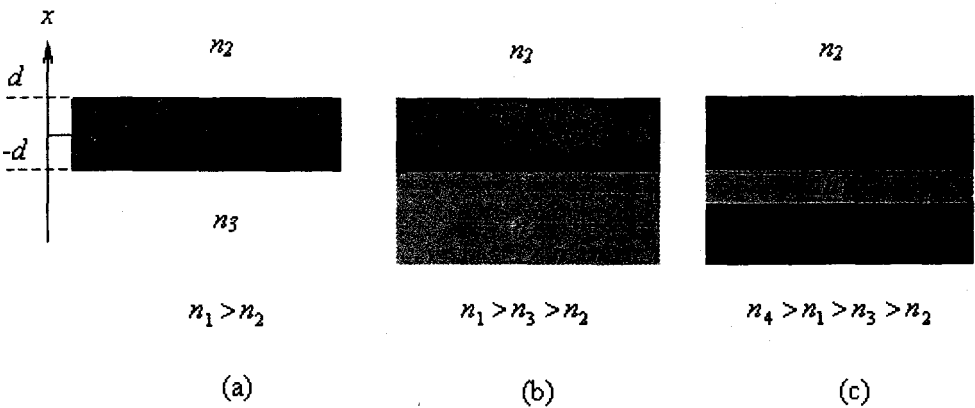


Figure 2.4. Types of dielectric slab waveguides, (a) Symmetrical waveguide, (b) Asymmetrical waveguide and (c) Anti-reflection resonant optical waveguide (ARROW)

The modes of a dielectric slab waveguide shown in Figures 2.4 are hybrid modes in general, but they can be decomposed into quasi-transverse electric (TE) and quasi-transverse magnetic (TM) modes.

A quasi-TE polarized light has one magnetic field component that is pointed out of the propagation plane and two electric field components which are within the plane. Quasi-TM polarized light has one electric field component pointing out of the plane and two magnetic field components which are within the plane. The wave equations (with x - z propagation plane) for quasi-TE mode are

$$\frac{\partial^2 H_y}{\partial x^2} + (k_0^2 n^2 - \beta^2) H_y = 0 \quad (2.19)$$

$$E_x = \frac{\beta}{\omega \epsilon} H_y \quad (2.20)$$

$$E_z = -\frac{i}{\omega \epsilon} \frac{\partial H_y}{\partial x} \quad (2.21)$$

and the wave equations for quasi-TM mode are

$$\frac{\partial^2 E_y}{\partial x^2} + (k_0^2 n^2 - \beta^2) E_y = 0 \quad (2.22)$$

$$H_x = -\frac{\beta}{\omega \mu_0} E_y \quad (2.23)$$

$$H_z = \frac{i}{\omega \mu_0} \frac{\partial E_y}{\partial x} \quad (2.24)$$

Typical field solutions for quasi-TM modes, assuming an asymmetrical slab structure shown in Figure 2.4(b), are shown in Figure 2.5. The dispersion diagram and the dependence of propagation constant on frequency is plotted in Figure 2.6. The modal propagation constant of the modes supported by the waveguide increases as the operating frequencies is increased. At lower frequencies (higher wavelengths)

the modes would couple into the radiation mode region. However in the forbidden region, no guided mode would be found as the fundamental mode effective index cannot be larger than the bulk refractive index of the core layer in the waveguide.

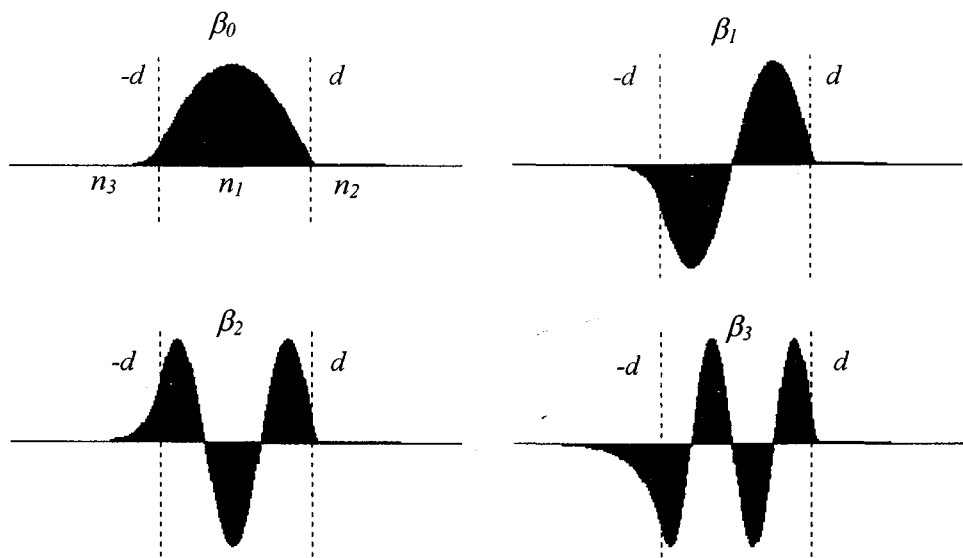


Figure 2.5. Typical field profiles of the first four quasi-TM modes supported in a asymmetric slab waveguide shown in Figure 2.4(b). Typical propagation constants of the modes would have its propagation constants, $\beta_0 > \beta_1 > \beta_2 > \beta_3$.

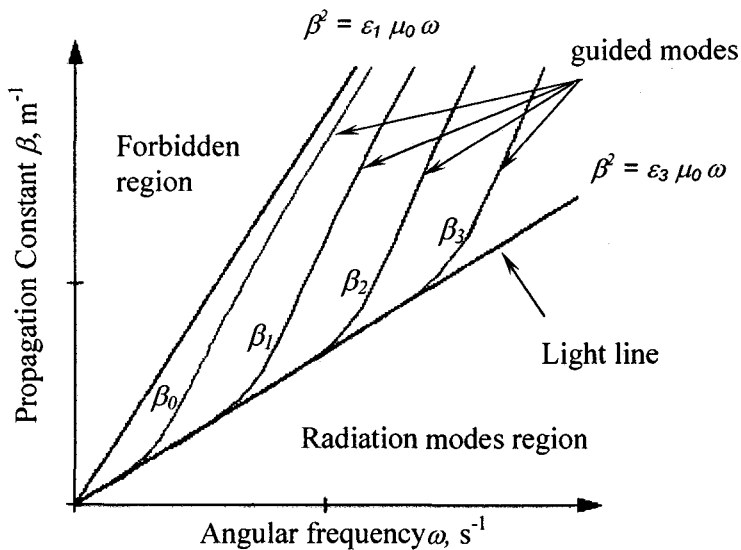


Figure 2.6. A typical dispersion diagram for quasi-TM modes in a dielectric slab waveguide: shown in terms of propagation constant and angular frequency.

2.1.2 Mode Expansion

Apart from the discrete set of guided modes, radiation modes and leaky modes are also solutions to Maxwell equations. Radiation modes form a continuum and having the property $k_0^2 n_2^2 < \beta^2 < k_0^2 n_3^2$ for substrate radiation modes and $\beta^2 < k_0^2 n_2^2$ for true radiation modes. A detailed discussion of radiation modes can be found in reference [69]. Leaky modes are also radiation modes but they are considered as a continuation of guided modes, since they will become part of guided modes as the frequency (wavelength) increases (decreases), seen as the guided modes dispersion curves extending into the radiation modes region, as shown in Figure 2.6. The guided modes together with the radiation modes form a complete orthogonal set.

2.2 Coupled Waveguide Array

In coupled waveguide array, the array mode is described as a collective excitation or a “supermode” of the individual waveguides modes, evanescently coupled to each other [71,72]. The supermode is described in terms of the individual modes complex amplitudes, with the details of the field between the waveguides contained in the coupling constant. A more general approach, in which waveguide arrays are regarded as an example of a general one-dimensional periodic optical structure, is the Floquet-Bloch (FB) analysis [73]. It predicts that the propagation-constant spectrum of the array’s eigenmodes is divided into bands, separated by gaps in which propagating modes do not exist.

Considering the case of three parallel waveguides as illustrated in Figure 2.7, suppose that the central direction of propagation is in the direction of z-axis, i.e. 90° normal to the direction of periodicity, the periodic dielectric permittivity given as

$$\varepsilon(x) = \varepsilon(x + a) \quad (2.25)$$

with a being the periodic lattice constant.

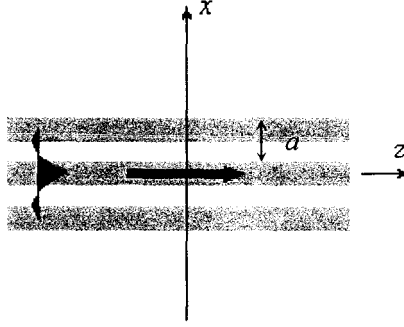


Figure 2.7. Two-dimensional view of arrayed waveguides in parallel made of a layered structure. The direction of wave propagation is 90° normal to the direction of periodicity.

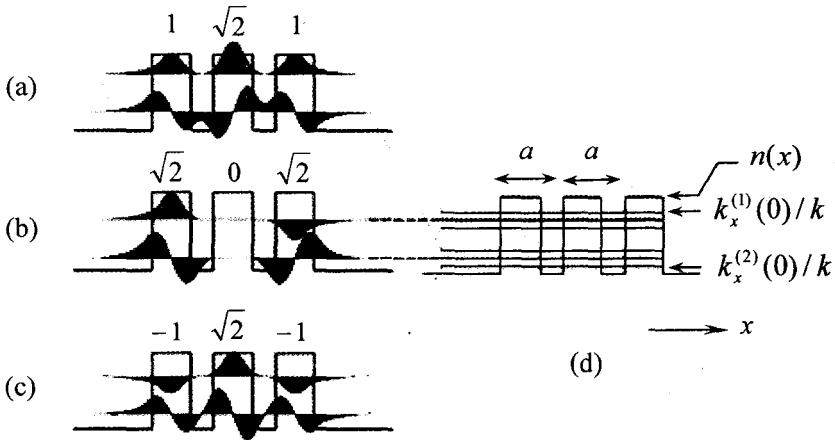


Figure 2.8. Mode patterns of orthogonal modes when three parallel waveguides are brought close for directional coupling. (a)–(c): The field profiles for the six lowest-order guided modes for the index structure of three coupled waveguides. (d) The relative magnitudes of $k_x^{(b)}/k$ positioned with respect to $n(x)$, the refractive-index profile of three coupled waveguides [72].

The amplitude patterns of guided modes created by bringing the three guides closely are schematically illustrated in Figures 2.8(a), (b) and (c) [72]. The three propagation constants diverge from the original value of an isolated waveguide as the

three guides are put closer. A typical dispersion diagram shown in Figure 2.9 is for three waveguide arrays clearly show the mode splitting as a result of coupling between adjacent waveguides. If we increase the number of parallel waveguides in the array, the diverging propagation constants form a near continuum which is called a band.

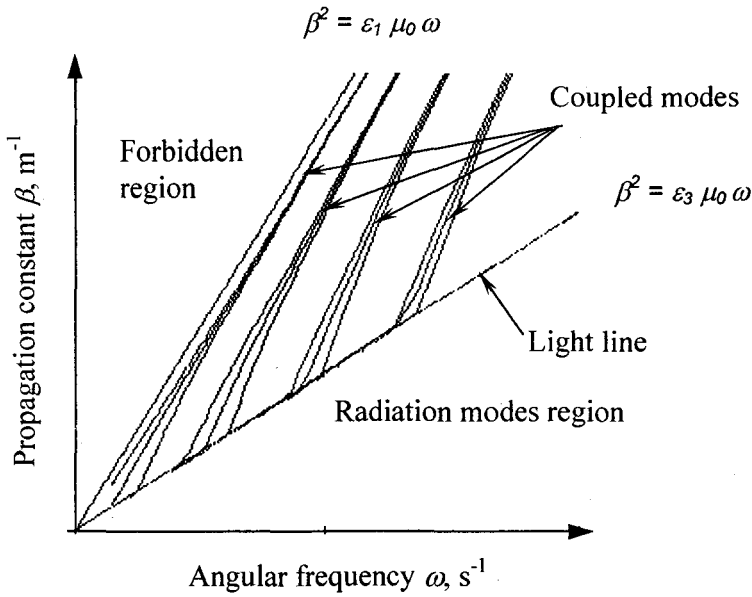


Figure 2.9. A typical dispersion diagram for TM modes in a coupled dielectric waveguide as in Figure 2.8. As the three coupled waveguides are put closer, the three propagation constants diverge from the original value of an isolated waveguide, depicted in Figure 2.6.

2.2.1 Photonic Band Diagram of 1-D Periodic Structure

The one-dimensional arrays of high and low refractive index material would exhibit eigenmodes divided into bands, separated by gaps in which propagating modes do not exist. Suppose the periodic dielectric array as shown in Figure 2.10 is consisted of a polymeric compound [74] of high refractive index ($n = 1.59$) layer of width d , and low refractive index ($n = 1.0$) layer of width s . The period for the layer is $a = d + s$.